ACS APPLIED MATERIALS & INTERFACES

www.acsami.org

Research Article

Self-Assembled Benzotriazole Interlayer Stabilizes ZnO/Polymer Interfaces Enables Thermally Robust Organic Solar Cells

Qian Xi,[⊥] Jiajun Hong,[⊥] Jian Qin, Muhammad Jawad, Na Wu, Oskar J. Sandberg, Rong Huang, Zhiyun Li, Ronald Österbacka, and Chang-Qi Ma*

Cite This: *ACS Appl. Mater. Interfaces* 2025, 17, 66673−66682

Read Online

ACCESS | Metrics & More | Article Recommendations | Supporting Information

ABSTRACT: Improving the thermal stability of organic solar cells (OSCs) is essential for advancing their practical deployment. In this paper, the thermal stability of organic solar cells was significantly improved by a benzotriazole (BTA) molecular layer assembled at the ZnO/active layer interface, introduced by spin-coating on the polymer blend surface. Experimental results demonstrated that BTA modification effectively suppressed the diffusion of MoO_3 and its interaction with ZnO, thereby mitigating energy-level mismatch and interfacial recombination. Remarkably, the BTA-modified device retained 86% of its initial efficiency following prolonged thermal aging at 85 °C for 1000 h, compared to 70% for unmodified devices. Detailed analysis via X-ray photoelectron spectroscopy (XPS) and ultraviolet photoelectron spectroscopy (UPS) revealed that BTA reduced adsorbed oxygen content on ZnO and lowered its work function, facilitating improved charge transport. This study provides a solution-processable interfacial engineering strategy for enhancing OSC stability under practical operating conditions.

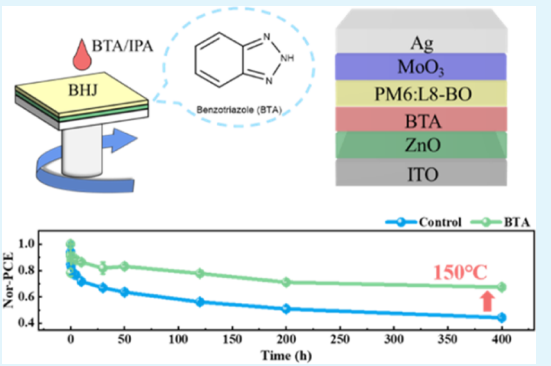

KEYWORDS: *organic solar cells, thermal stability, benzotriazole (BTA), ZnO/active layer interface, MoO_3 diffusion, interfacial engineering*

Downloaded via 58.211.88.98 on January 4, 2026 at 03:46:40 (UTC).
See https://pubs.acs.org/sharingguidelines for options on how to legitimately share published articles.

INTRODUCTION

Organic solar cells (OSCs) have garnered significant attention due to their lightweight,[1] flexibility,[2] and compatibility with large-area printing processes.[3] While state-of-the-art OSCs have reached ≈21% PCE for single-junction small-area cells (0.04 cm^2) and certified ∼20.8% on large-area 1 cm^2 cells, monolithically interconnected mini-modules have achieved 17.0% at 17.6 cm^2,[4−7] their stability remains a critical barrier to commercialization.[8,9] The degradation mechanisms of OSCs are broadly categorized into extrinsic (oxygen/moisture ingress)[10,11] and intrinsic factors (thermal- and light-induced changes).[12−15] The encapsulation of solar cells serves as an effective barrier against moisture and oxygen ingress,[16] while degradation induced by light and heat is typically mitigated through interfacial engineering.[17]

The performance and stability of OSCs are closely related to the selection of interfacial layer materials. Common electron transport layer (ETL) materials for cathode interfaces include ZnO,[18] SnO_2,[19] and organic small molecules,[20] which help to reduce the work function at the electrode interface, thereby facilitating charge extraction and transport efficiency. However, ZnO exhibits photocatalytic properties and can generate free radicals under light irradiation, leading to the degradation of nonfullerene acceptor (NFA) materials.[21] In recent years, organic ETL materials have gained attention. For instance, diphenylquinoline (DPC), compared to conventional bathocuproine (BCP), exhibits enhanced steric hindrance and stronger electron-withdrawing ability, effectively suppressing interfacial reactions with NFAs and improving photothermal stability.[22] Additionally, benzamide-functionalized H75 demonstrates superior thermal stability at elevated temperatures, outperforming conventional PDIN and PDINN materials.[23]

In OSCs, a variety of interfacial materials have been employed as hole transport layers (HTLs) to facilitate efficient hole extraction and improve device performance. Representative conductive polymers such as poly(3,4-ethylenedioxythiophene)/poly(PEDOT/PSS),[24] two-dimensional (2D) materials including molybdenum disulfide (MoS_2),[25] transition metal oxides such as nickel oxide (NiO_x),[26] and self-assembled monolayer (SAM) molecules like 2-(9H-carbazol-9-yl)ethyl)-phosphonic acid (2-PACz)[27] have been extensively explored. Despite these materials can smooth the interfacial charge injection and consequently improve device performance, they

Received: September 12, 2025
Revised: November 13, 2025
Accepted: November 20, 2025
Published: November 27, 2025

ACS Publications

© 2025 American Chemical Society

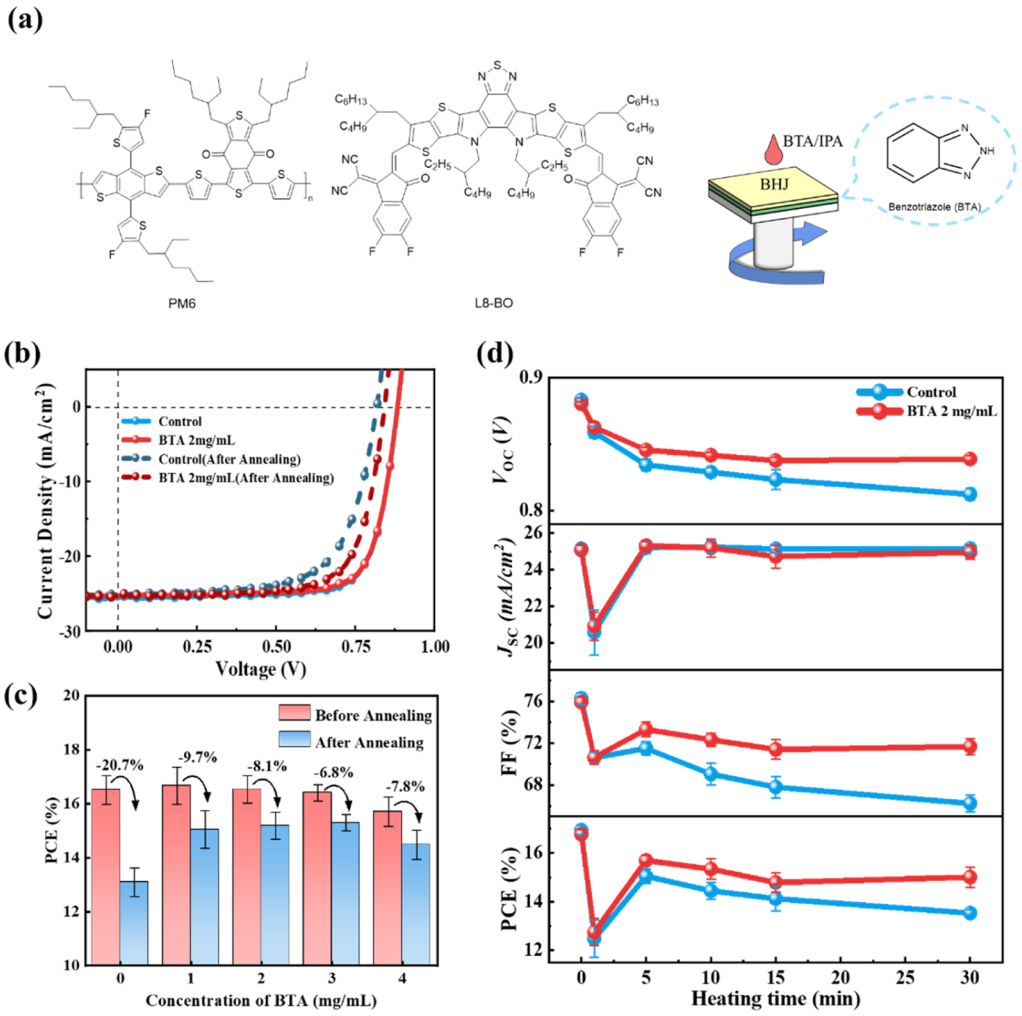

Figure 1. (a) Chemical structures of PM6, L8-BO, and BTA, along with a schematic representation of the deposition of BTA on bottom of the PM6:L8-BO; (b) current density−voltage (J−V) curves of the 2 mg/mL BTA-modified device and the control device, measured before and after thermal annealing at 150 °C for 30 min; (c) initial PCE and PCE loss after 150 °C annealing for 30 min for devices with different BTA concentrations; (d) evolution of the device performance for the 2 mg/mL BTA-modified and control devices upon 150 °C annealing.

also introduce stability challenges to the cells.[28] As an example, the most commonly used hole transport layer, MoO_3 has been identified as a key issue to thermal instability due to its propensity to diffuse into the active layer and accumulate at the ZnO interface under prolonged annealing, which induces p-doping at the photoactive layer/MoO_3 interface, interfacial energy-level misalignment, and accelerated charge recombination.[29]

In this work, a small molecule benzotriazole (BTA) was found to be able to improve the thermal stability of inverted polymer/nonfullerene solar cells having ZnO electron transporting layer. Although BTA was deposited onto the polymer blend film via spin coating, accumulation of BTA at the polymer/ZnO interface was confirmed by ToF-SIMS. XPS and UPS analyses demonstrated that the self-assembled BTA reduces the work function of the ZnO layer and passivate the oxygen vacancies. Most importantly, this BTA layer prevents the direct contact of diffused MoO_3^- species at the ZnO surface, which facilitates the electron transfer at the interface and consequently improves the performance of the cell upon thermal annealing. Coupled with the use of TCTA as the protection layer at the MoO_3/polymer interface,[29] the BTA incorporated cells exhibited improved long-term thermal stability, retaining 86% of their initial power conversion efficiency after sequential thermal stress tests: thermal encapsulation at 150 °C for 30 min followed by annealing at 85 °C for 1000 h. The current research work gives a deep insight into the thermal-induced performance decay of the cells and provides an effective method to improve device stability.

RESULTS AND DISCUSSION

Suppression of Thermal Degradation via BTA Modification. Figure 1a presents the chemical structures of PM6, L8-BO, and BTA, along with a schematic illustration of the BTA deposition process. Devices treated with pure isopropanol were labeled as control devices, while those incorporating isopropanol-based BTA solutions at different concentrations were referred to as BTA-treated devices. To investigate the impact of BTA concentration, devices were fabricated using BTA solutions ranging from 1 mg/mL to 4 mg/mL, and their J−V curves were measured. The photovoltaic parameters are summarized in Table S1. The control cell without BTA treatment exhibited an average power conversion efficiency (PCE) of 16.51%, with a peak efficiency of 17.27%, which is comparable to the literature reports,[30] suggesting that the cells were well optimized. Devices treated

https://doi.org/10.1021/acsami.5c18226
ACS Appl. Mater. Interfaces 2025, 17, 66673−66682

Table 1. Photovoltaic Performance of 2 mg/mL BTA-Modified and Control Devices after 150 °C Annealing for 30 min

interlayer	annealing time (min)	V_{OC} (V)[a]	J_{SC} (mA/cm^2)[a,b]	FF (%)[a]	PCE (%)[a]	PCE_{max} (%)[c]
control	0	0.883 ± 0.002	25.14 ± 0.25	76.28 ± 0.56	16.94 ± 0.18	17.15
	1	0.859 ± 0.004	20.58 ± 1.23	70.62 ± 0.54	12.48 ± 0.77	13.28
	3	0.834 ± 0.004	25.22 ± 0.32	71.50 ± 0.66	15.04 ± 0.30	15.57
	5	0.829 ± 0.003	25.24 ± 0.33	69.04 ± 1.05	14.45 ± 0.34	14.81
	10	0.823 ± 0.007	25.13 ± 0.22	67.80 ± 1.03	14.12 ± 0.50	15.21
	30	0.812 ± 0.004	25.16 ± 0.21	66.23 ± 0.81	13.53 ± 0.14	13.74
BTA (2 mg/mL)	0	0.880 ± 0.002	24.56 ± 0.54	75.93 ± 0.48	16.77 ± 0.20	17.04
	1	0.863 ± 0.004	20.93 ± 0.77	70.64 ± 0.64	12.75 ± 0.55	13.92
	3	0.846 ± 0.002	25.32 ± 0.24	73.32 ± 0.69	15.70 ± 0.19	16.05
	5	0.842 ± 0.002	25.19 ± 0.49	72.33 ± 0.62	15.34 ± 0.42	15.71
	10	0.837 ± 0.003	24.72 ± 0.63	71.41 ± 0.95	14.79 ± 0.40	15.39
	30	0.839 ± 0.002	24.95 ± 0.38	71.68 ± 0.75	15.00 ± 0.41	15.44

[a]Device performance data averaged from 8 individual cells. [b]Short circuit current measured under simulated AM 1.5G sun light, which was calibrated with a certified Si cell. [c]Maximum PCE of the best cell.

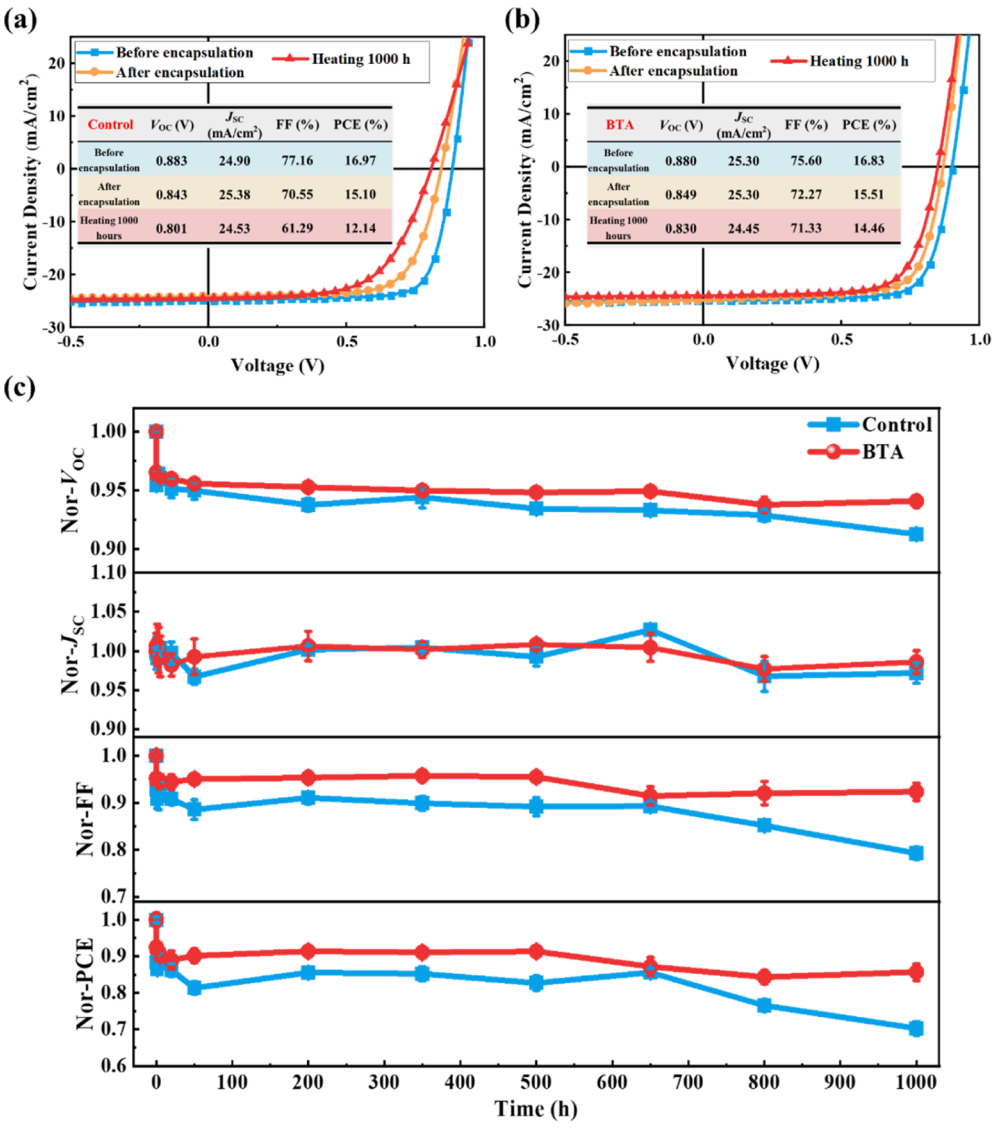

Figure 2. Encapsulation and long-term thermal stability of OSCs: (a) $J-V$ curves of the control device before and after encapsulation; (b) $J-V$ curves of the BTA-modified device before and after encapsulation; (c) comparison of long-term stability at 85 °C for 1000 h.

with lower BTA concentrations (1 and 2 mg/mL) exhibited average PCEs of 16.66% and 16.53%, respectively, indicating negligible influence on the initial device performance. However, when the BTA concentration increased to 3 mg/mL, PCE slightly declined to 16.40%, primarily due to a decrease in FF (Figure S1 and Table S1). At 4 mg/mL, both

https://doi.org/10.1021/acsami.5c18226
ACS Appl. Mater. Interfaces 2025, 17, 66673−66682

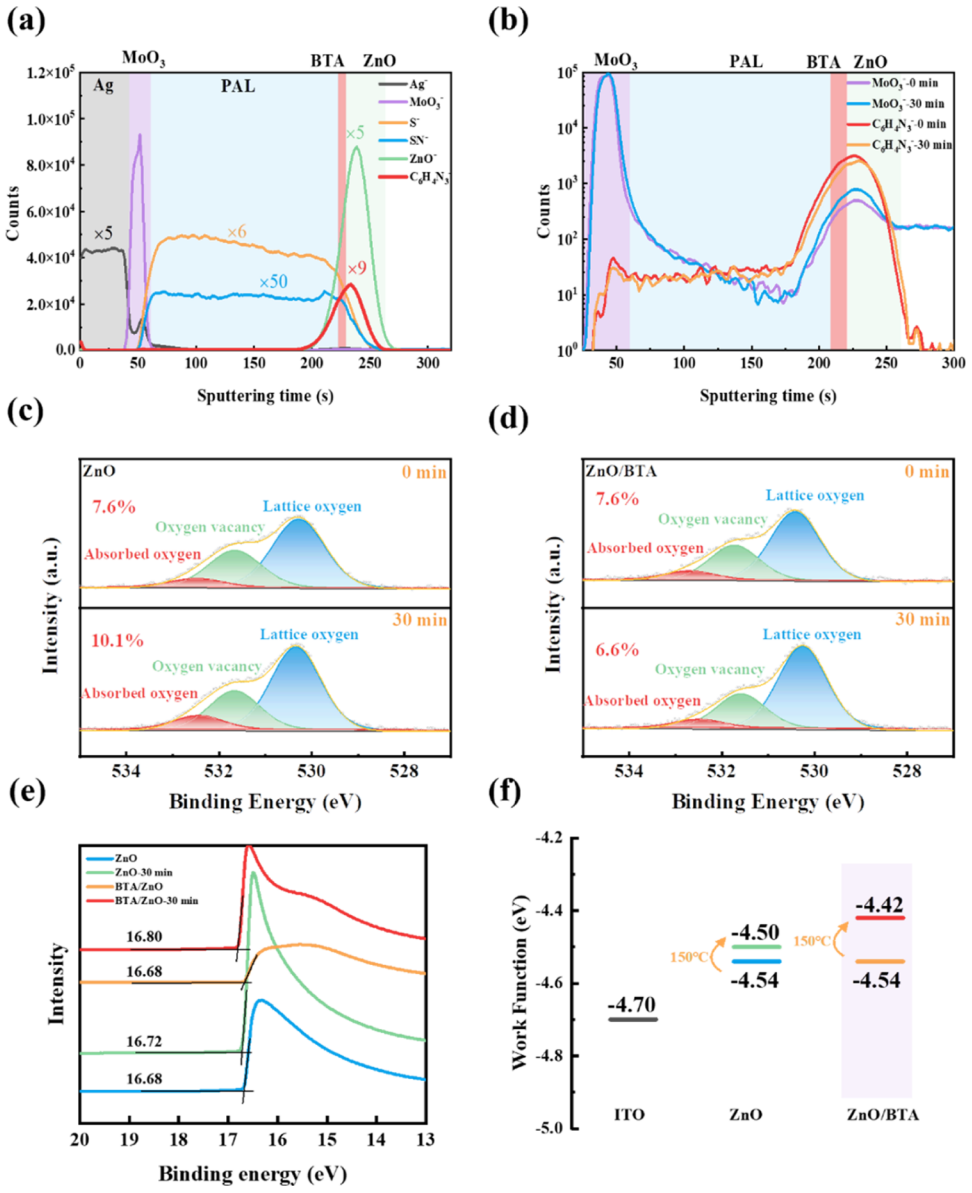

Figure 3. (a) TOF-SIMS depth profile of anion fragments in a BTA-modified device with a structure of ITO/ZnO/PM6:L8-BO/MoO_3/Ag; (b) depth distribution of MoO_3^- (representing MoO_3) and $C_6N_4H_3^-$ (representing BTA) before and after thermal annealing of the semidevice of ITO/ZnO/PM6:L8-BO/MoO_3, note that the *y*-axis is in a logarithmic scale; (c) O 1s XPS spectra of ZnO before and after annealing; (d) O 1s XPS spectra of BTA-modified ZnO before and after annealing; (e) UPS spectra of ZnO and BTA/ZnO films before and after annealing. (f) Variation of the work function of the two films as a function of annealing time.

V_{OC} and FF significantly decreased, resulting in a PCE drop to 15.70%. These results suggest that BTA concentrations below 2 mg/mL have minimal impact on the initial device efficiency.

To evaluate the thermal stability of OSCs with different BTA concentrations, we subjected the devices to thermal annealing at 150 °C for 30 min and monitored their photovoltaic performance. 150 °C was chosen as an accelerated diagnostic temperature to activate MoO_3/organic interfacial degradation and thus maximize sensitivity to BTA-dependent stabilization.[31] The evolution of the device performance for the 2 mg/mL BTA-treated and control cells is depicted in Figure 1d, and the photovoltaic performance data are listed in Table 1. The full comparison of all five cells is presented in Figure S1 and Table S1, respectively. As seen from here, for the device without BTA treatment, V_{OC} and FF exhibited continuous degradation over time, while J_{SC} decreased sharply within the first minute of annealing, partially recovered by the fifth minute, and then remained stable. This is attributed to the p-type doping in the active layer of the diffused MoO_3^- species.[29] The persistent decline of V_{OC} and FF leads to a more than 20% PCE decrease for the control device upon annealing, indicating that isopropanol alone does not provide noticeable thermal stabilization. In contrast, devices with BTA exhibited significantly reduced V_{OC} and FF degradation, maintaining stable values after 10 min of annealing. As the BTA concentration increased to 3 mg/mL, the thermal stabilization effect improved, with the PCE loss reduced to 6.8% after 30 min of annealing (Figure 1c). Notably, the 4 mg/mL BTA-modified device exhibited a slightly higher PCE loss of 7.8%, suggesting that an optimal concentration is required for maximum thermal stability. Among all tested concentrations, 2 mg/mL BTA provided the

https://doi.org/10.1021/acsami.5c18226
ACS Appl. Mater. Interfaces 2025, 17, 66673−66682

best balance between high initial efficiency and thermal stability, making it the most suitable concentration for practical applications.

To further investigate the effect of BTA modification on the thermal stability of the devices, we compared the thermal degradation of the 2 mg/mL BTA device with that of the control device. Figure 1b shows the $J-V$ curves of the 2 mg/mL BTA-modified and control devices, measured before and after thermal annealing at 150 °C for 30 min. As shown in Figure 1d, the BTA-modified device exhibited moderate degradation within the first 5 min of annealing, where V_{OC} and FF dropped from 0.880 to 0.846 V and from 75.93% to 73.32%, respectively. This initial degradation trend was similar to that of the control device. However, after 30 min of annealing, the BTA-modified device showed significantly improved stability, with V_{OC} and FF retained at 0.839 V and 71.68%, whereas in the control device, these parameters declined to 0.812 V and 66.23%, respectively. Overall, after 30 min at 150 °C, the BTA-modified device maintained an average PCE of 15.00%, significantly higher than the 13.53% of the control device.

Since the 150 °C thermal stability test demonstrated that the 2 mg/mL BTA device exhibits the least efficiency loss under high-temperature annealing, we further tested its stability after encapsulation and prolonged thermal aging at 85 °C. To investigate the encapsulation stability, standard and BTA-modified OSCs were encapsulated via hot pressing at 120 °C for 5 min. The $J-V$ curves before and after encapsulation are shown in Figure 2. For the control device, PCE dropped from 16.97% to 15.10% after encapsulation, whereas the BTA-modified device exhibited a milder decline from 16.83% to 15.51%, suggesting that BTA does not significantly mitigate the immediate thermal degradation during short-term annealing. Subsequently, the encapsulated devices were subjected to long-term thermal aging at 85 °C. As shown in Figure 2, BTA modification substantially improved long-term stability. The BTA-modified device retained 86% of its initial PCE after 1000 h, whereas the control device retained only 70%. This improvement was attributed to the slower degradation rates of V_{OC} and FF in BTA-modified devices. These results demonstrate that BTA modification provides an effective and practical approach to enhancing the thermal stability of OSCs, making it a promising candidate for applications.

Effect of BTA on the ZnO Interface. To examine whether spin-coating BTA solution affects the active layer, we compared the UV−vis absorption spectra of PM6:L8-BO films under three conditions: untreated, treated with isopropanol (IPA) and treated with 2 mg/mL BTA (BTA). As shown in Figure S2, the three films exhibited nearly identical absorption spectra before annealing, with no significant changes in peak positions or intensities, suggesting that BTA modification does not induce chemical reactions or morphological alterations in the active layer. Although initially similar, all films exhibited a slight redshift in the acceptor absorption peak (~790 nm) after thermal annealing at 150 °C (Figure S2), indicating thermally induced molecular ordering.[32] However, the spectral differences among the three films remained negligible, confirming that BTA modification does not disrupt the morphology or molecular arrangement of the active layer.

To further understand the impact of BTA on device performance during thermal aging, we employed time-of-flight secondary ion mass spectrometry (TOF-SIMS) to analyze the elemental distribution in the devices. Figure 3a presents the depth profiles of characteristic fragment ions in BTA-modified devices. Since the SN^- and $C_6N_4H_3^-$ signals originate exclusively from L8-BO and BTA, respectively, their depth distributions represent the locations of L8-BO and BTA. The data reveal that BTA molecules, although initially spin-coated onto the active layer, predominantly accumulate at the ZnO interface even before thermal annealing. Such enrichment is attributed to transient permeation of small polar BTA molecules through the solvent-plasticized PM6:L8-BO free volume during spin-coating, followed by triazole−Zn coordination and interfacial hydrogen bonding that lower the interfacial free energy and promote self-assembly on ZnO. Figure 3b compares the TOF-SIMS depth profiles of the MoO_3^- fragments and the BTA related $C_6N_4H_3^-$ fragments before and after thermal annealing. The BTA signal displays a confined interfacial maximum with baseline levels throughout the bulk photoactive layer and is absent in BTA-free controls, a behavior incompatible with sputter-induced tailing, which would smear the signal into the bulk rather than produce a sharp interfacial peak. Figure S3 shows the MoO_3^- depth-profile comparison for full cells with and without BTA: the control displays higher MoO_3^- counts encroaching into the PAL, whereas the BTA-treated device exhibits a steeper decay at the PAL/BTA boundary and lower MoO_3^- levels within the PAL. Consistent with previous studies,[29] MoO_3 diffusion was detected even in as-fabricated devices, where a small but noticeable amount of MoO_3^- already accumulated at the ZnO/active layer interface. After 30 min of annealing at 150 °C, the MoO_3^- profile broadened, and its intensity increased at the ZnO interface, confirming continuous MoO_3^- diffusion. However, the depth distribution of $C_6N_4H_3^-$ (BTA) remained stable before and after annealing, indicating that BTA forms a self-assembled interlayer on ZnO that blocks direct chemical contact with MoO_3^- derived reduced species at the ZnO/active interface, thereby passivating the interface and mitigating interfacial degradation pathways under thermal stress.

To further examine the interfacial interaction between BTA and ZnO, we conducted X-ray photoelectron spectroscopy (XPS) measurements. Figure 3c,d presents the O 1s spectra of pristine ZnO and BTA-modified ZnO films before and after thermal annealing. The O 1s peak in ZnO can be deconvoluted into three components: lattice oxygen (530.1 eV), oxygen vacancies (531.2 eV), and adsorbed oxygen (532.0 eV).[33] As shown in Figure 3c,d, in the as-fabricated films, BTA modification does not significantly alter the proportion of the three oxygen species, with the adsorbed oxygen content at approximately 7.6%. However, after thermal annealing at 150 °C, the adsorbed oxygen level in pristine ZnO increased to 10.1%, whereas in BTA-modified ZnO, it remained as low as 6.6%. This suggests that BTA suppresses the formation of additional adsorbed oxygen species, which are known to act as charge traps and degrade device performance.

To investigate the effect of BTA modification on the energy levels, we performed ultraviolet photoelectron spectroscopy (UPS) measurements on ZnO and BTA-modified ZnO before and after annealing. Figure 3e presents the UPS spectra of the Fermi edges, and Figure 3f shows the corresponding work function values. Before thermal annealing, both pristine ZnO and BTA-modified ZnO exhibited a similar work function of 4.54 eV. However, after 150 °C annealing, the work function of pristine ZnO remained almost unchanged at 4.50 eV, whereas BTA-modified ZnO exhibited a notable decrease to 4.42 eV.

https://doi.org/10.1021/acsami.5c18226
ACS Appl. Mater. Interfaces 2025, 17, 66673−66682

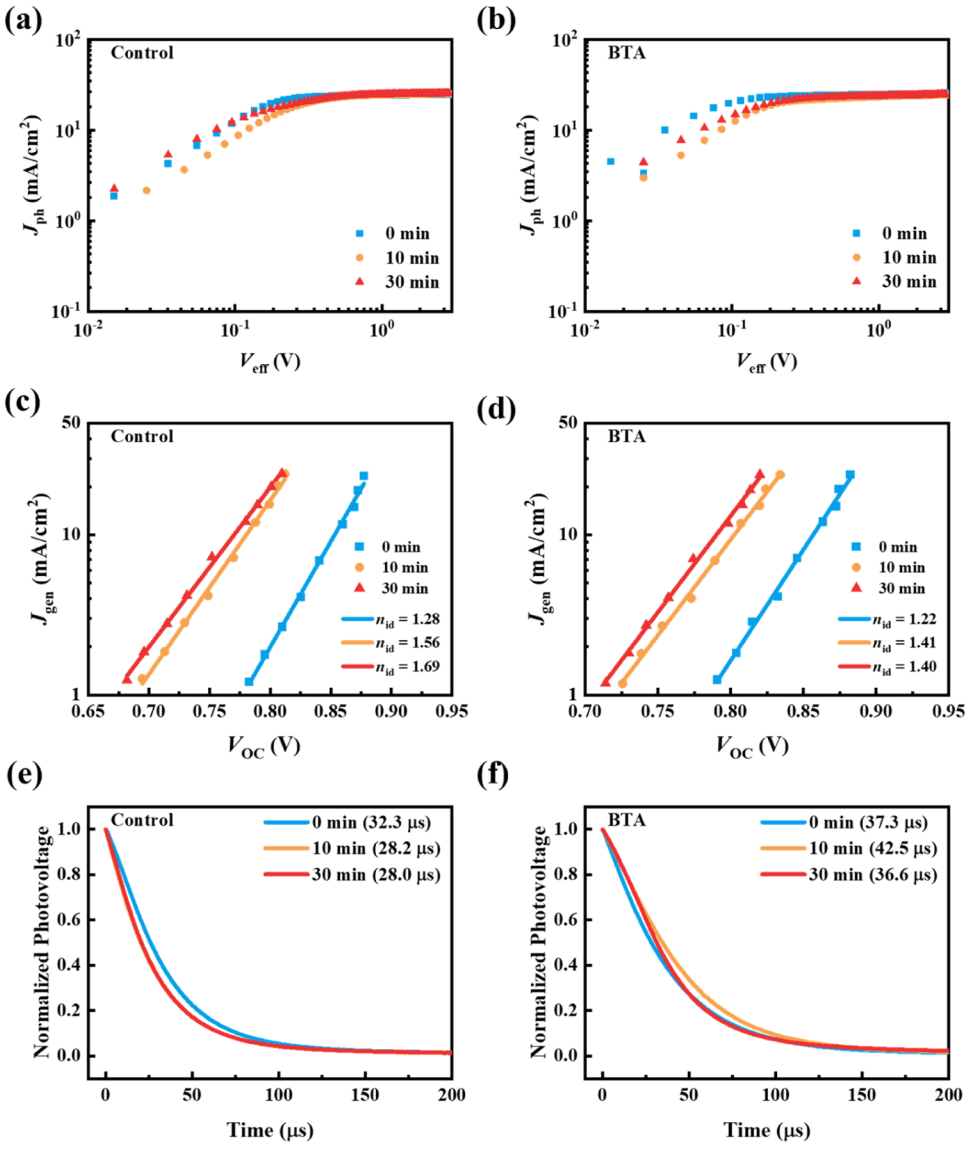

Figure 4. J_{ph}-V_{eff} curves for (a) control and (b) BTA-modified devices under annealing; j_{gen}-V_{OC} relationships for (c) control and (d) BTA-modified devices under annealing; TPV-derived carrier lifetimes for (e) control and (f) BTA-modified devices under annealing.

The reduction in work function suggests that BTA facilitates the formation of an ohmic contact at the ZnO/active layer interface, thereby improving charge extraction efficiency and mitigating the effects of MoO_3 diffusion-induced energy level misalignment. Beyond the cutoff, the valence-band/Fermi-edge region was further analyzed (Figure S4). The spectra show that the valence-band edge of bare ZnO slightly shifts after annealing, whereas that of BTA-modified ZnO remains nearly unchanged, confirming that BTA helps maintain a stable surface electronic structure under thermal stress.

Influence of BTA Modification on Charge Extraction and Recombination. To validate the proposed mechanism and comprehensively understand the impact of BTA modification on charge collection and carrier transport, further electrical characterization was conducted to investigate charge extraction and recombination dynamics. Figure 4a-b displays the photogenerated current density (J_{ph}) versus effective voltage (V_{eff}) curves for control and BTA-modified devices under 150 °C annealing for 0, 10, and 30 min. Here, V_{eff} is defined as the difference between the applied voltage and V_0, where V_0 corresponds to the voltage at which J_{ph} equals zero. The charge collection efficiency (P_{coll}) was estimated by the ratio of J_{ph} at short-circuit conditions to the saturated J_{ph}.[34,35] Both devices exhibited flat J_{ph}-V_{eff} curves at V_{eff} over 2 V, independent of annealing time (Figure 4a,b), indicating efficient charge extraction even after prolonged thermal stress. This behavior aligns with the absence of BTA doping within the active layer and its role in optimizing interfacial energy-level alignment.

The recombination dynamics were further probed using the Suns-V_{OC} method.[36] The relationship between V_{OC} and the generated current density (j_{gen}) follows eq 1, where n_{id} (recombination ideality factor) was derived.

$$j_{gen} = j_0 \exp^{(eV_{OC}/n_{id}kT)} \quad (1)$$

Figure 4c,d illustrates the logarithmic correlation between j_{gen} and V_{OC}. The corresponding light-intensity-dependent $J-V$ curves are provided in the Figure S5. For control devices, n_{id} increased from 1.28 to 1.56 after 10 min of annealing, signifying a surge in trap-assisted recombination. Prolonged

https://doi.org/10.1021/acsami.5c18226
ACS Appl. Mater. Interfaces 2025, 17, 66673−66682

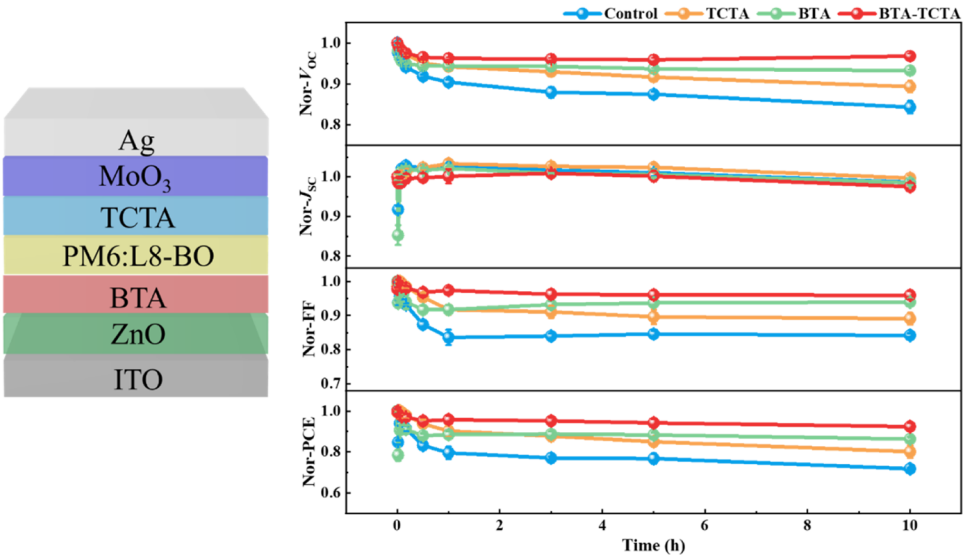

Figure 5. Thermal stability (150 °C/10 h) of control, TCTA-, BTA-, and TCTA-BTA-modified devices.

annealing (30 min) further elevated n_{id} to 1.69, albeit at a reduced rate, reflecting partial stabilization. In contrast, BTA-modified devices showed a smaller n_{id} increase (1.22 to 1.41) after 10 min, stabilizing at 1.40 after 30 min, underscoring BTA's efficacy in suppressing defect-mediated recombination during extended thermal exposure.

Transient photovoltage (TPV) measurements quantified carrier lifetimes (Figure 4e,f). Fresh control and BTA devices exhibited lifetimes of 32.3 and 42.5 μs, respectively. After 10 min of annealing, lifetimes decreased to 28.2 μs (control) and 37.3 μs (BTA). By 30 min, further reductions to 28.0 μs (control) and 36.6 μs (BTA) were observed, consistent with a "burn-in" degradation pattern. Notably, BTA devices consistently retained longer lifetimes throughout annealing, validating its role in mitigating carrier recombination.

Thermal Stability Improvement of OSCs by Bilateral Protection. These results collectively demonstrate that BTA modification preserves charge collection efficiency while reducing thermally induced defect recombination, thereby enhancing carrier lifetime and device stability. To optimize stability, dual-interface modification with BTA (ZnO side) and TCTA (MoO_3 side), which has been reported in our previous study,[25] was implemented. As shown in Figure S6, cells without HTL interface protection (both the reference and BTA-based cells) exhibited an initial rapid decay followed by partial recovery during the first 30 min of thermal stress at 150 °C. In contrast, this short-term instability was effectively suppressed in the TCTA-modified devices, regardless of the BTA modification. The almost identical decay behavior of the TCTA-modified cells indicates that the initial performance decay of the TCTA-free cells is mainly due to the unsatisfied HTL/polymer interface. As reported in our previous study,[25] brief heating at 150 °C causes partial reduction of MoO_3 and diffusion of MoO_3^- species into the active layer, which leads to a temporary decrease of J_{SC}. With prolonged annealing, these species migrate toward the cathode, resulting in partial recovery. A thin TCTA layer blocks this diffusion and thus suppresses the transient J_{SC} decay. Figure 5 depicts the performance decay of the cells upon 10 h thermal annealing at 150 °C. In such a time scale, the TCTA and BTA comodified devices retained 92% of their initial PCE, significantly surpassing the standalone BTA (86%) and TCTA (80%) devices. This synergy highlights BTA's ability to block hole-transport material diffusion at the ZnO interface, reduce interfacial recombination, and lower energy barriers. Critically, BTA effectively addresses the limitations associated with TCTA, which suffers from interfacial diffusion and energy-level misalignment during prolonged annealing. Moreover, the long-term data in Figure S7 show that the comodified devices still maintained 72% of their initial PCE even after 400 h of continuous annealing, highlighting their markedly improved long-term stability compared to BTA (67%) and TCTA (44%) counterparts.

SUMMARY

This work systematically elucidates the role of BTA in enhancing OSC thermal stability. At an optimal concentration (2 mg/mL), BTA minimally impacts initial PCE while significantly suppressing V_{OC} and FF degradation under prolonged annealing. BTA-modified devices encapsulated by hot pressing at 150 °C retained 86% of their initial power conversion efficiency after 1000 h of thermal annealing at 85 °C. TOF-SIMS, XPS, and UPS analyses confirm that BTA self-assembles at the ZnO interface, blocking (MoO_3) diffusion, reducing adsorbed oxygen, and lowering the ZnO work function (4.42 eV vs 4.54 eV for bare ZnO). Electrical characterization further reveals reduced trap-assisted recombination and prolonged carrier lifetimes in BTA devices. Dual modification with BTA and TCTA synergistically stabilizes both interfaces, retaining 72% PCE after 400 h at 150 °C. This work underscores the criticality of cathode interface engineering in OSC stability and provides a practical strategy for industrial-scale fabrication of durable photovoltaic devices.

METHODS

Device Fabrication. ITO substrates with a width of 3 mm were custom-fabricated on glass. The ITO-coated glass substrates were sequentially cleaned by ultrasonication for 40 min each in detergent, deionized water (twice), and ethanol (twice). After drying with nitrogen flow, the substrates were treated with O_2 plasma. Once cooled to room temperature, a ZnO precursor solution was prepared via a sol–gel method by dissolving zinc acetate dihydrate and ethanolamine in a 1:1 molar ratio in 2-methoxyethanol to a final

https://doi.org/10.1021/acsami.5c18226
ACS Appl. Mater. Interfaces 2025, 17, 66673−66682

concentration of 0.45 mol·L^{-1}. The ZnO solution was spin-coated onto the ITO substrates at 2000 rpm for 30 s, with an acceleration of 3000 rpm·s^{-1}. The coated films were then annealed at 200 °C for 30 min and transferred into a nitrogen-filled glovebox.

The active layer solution was prepared by blending PM6 and L8-BO at a weight ratio of 1:1.2 in chloroform containing 50 wt % 1,4-diiodobenzene, with a PM6 concentration of 7.2 mg·mL^{-1}. The mixture was stirred at 55 °C for 2 h and allowed to cool to room temperature before use. A 20 μL aliquot of the solution was spin-coated onto the substrate at 2000 rpm for 30 s. The resulting films were thermally annealed at 85 °C for 5 min and then cooled to room temperature. Subsequently, 15 nm of MoO_3 and 100 nm of Ag were thermally evaporated under high vacuum. For devices with BTA, after spin-coating the active layer film, an isopropanol solution of BTA at a defined concentration was drop-cast onto the film surface and dynamically spin-coated at 3000 rpm for 30 s. The film was subsequently thermally annealed at 85 °C for 5 min. All subsequent fabrication steps remained unchanged.

Solar Cell Measurement. *J*–*V Testing*. The current density–voltage (*J*–*V*) characteristics of the solar cells were measured using a digital source meter under simulated AM 1.5G illumination. The *J*–*V* curves, along with key device parameters such as open-circuit voltage (V_{OC}), short-circuit current density (J_{SC}), fill factor (FF), and power conversion efficiency (PCE), were recorded simultaneously using computer software. The active area of each device was 0.09 cm^2.

Thermal Stability Testing. Devices were thermally annealed at specific temperatures and durations on a heating stage inside a nitrogen-filled glovebox. After annealing, the devices were allowed to cool to room temperature prior to performance measurement.

Thermal Encapsulation. Device encapsulation was carried out using a hot press. The encapsulation temperature and duration were optimized experimentally and finalized at 120 °C for 5 min.

UV–Vis Absorption Spectroscopy. The solution was spin-coated onto bare glass substrates and thermally annealed to evaporate the solvent. UV–vis absorption spectra were recorded using a PerkinElmer Lambda 750 spectrophotometer.

Matrix-Assisted Laser Desorption/Ionization Time-of-Flight Secondary Ion Mass Spectrometry. SIMS measurements were conducted using a TOF-SIMS 5–100 instrument. Complete devices identical to those used for photovoltaic testing were fabricated and subjected to in situ annealing at 150 °C under high vacuum. Elemental distributions of Ag, Mo, O, S, Sn, and Zn were analyzed in the negative ion mode.

X-ray Photoelectron Spectroscopy. After the ZnO layer was prepared, a 2 mg/mL BTA solution in isopropanol was dynamically spin-coated onto its surface at 3000 rpm for 30 s, followed by thermal annealing at 85 °C for 5 min. XPS spectra were acquired using an ESCALAB 250Xi+ spectrometer equipped with a monochromatic Al Kα X-ray source. The binding energy was calibrated using the C–C peak of adventitious carbon as the reference.

Ultraviolet Photoelectron Spectroscopy. After the ZnO layer was prepared, a 2 mg/mL BTA solution in isopropanol was dynamically spin-coated onto its surface at 3000 rpm for 30 s, followed by thermal annealing at 85 °C for 5 min. UPS measurements were performed using an ESCALAB 250Xi+ spectrometer equipped with a monochromatic He I (21.2 eV) radiation source.

■ ASSOCIATED CONTENT

Supporting Information

The Supporting Information is available free of charge at https://pubs.acs.org/doi/10.1021/acsami.5c18226.

Device statistics for cells with different BTA concentrations; thermal annealing curves of photovoltaic parameters; UV–vis absorption spectra of PM6:L8-BO films; ToF-SIMS depth profiles of $MoO3^-$ with and without BTA; UPS valence-band analysis of ZnO and BTA/ZnO films; light-intensity-dependent *J*–*V* curves; short- and long-term thermal stability of devices with different interlayers (PDF)

■ AUTHOR INFORMATION

Corresponding Author

Chang-Qi Ma – *i-Lab & Printable Electronics Research Center, Suzhou Institute of Nano-Tech and Nano-Bionics, Suzhou 215123, P. R. China; School of Nano-Tech and Nano-Bionics, University of Science and Technology of China, Hefei 230026, P. R. China;* orcid.org/0000-0002-9293-5027; Email: cqma2011@sinano.ac.cn

Authors

Qian Xi – *i-Lab & Printable Electronics Research Center, Suzhou Institute of Nano-Tech and Nano-Bionics, Suzhou 215123, P. R. China; School of Nano-Tech and Nano-Bionics, University of Science and Technology of China, Hefei 230026, P. R. China*

Jiajun Hong – *i-Lab & Printable Electronics Research Center, Suzhou Institute of Nano-Tech and Nano-Bionics, Suzhou 215123, P. R. China*

Jian Qin – *i-Lab & Printable Electronics Research Center, Suzhou Institute of Nano-Tech and Nano-Bionics, Suzhou 215123, P. R. China; School of Nano-Tech and Nano-Bionics, University of Science and Technology of China, Hefei 230026, P. R. China*

Muhammad Jawad – *i-Lab & Printable Electronics Research Center, Suzhou Institute of Nano-Tech and Nano-Bionics, Suzhou 215123, P. R. China; School of Nano-Tech and Nano-Bionics, University of Science and Technology of China, Hefei 230026, P. R. China*

Na Wu – *i-Lab & Printable Electronics Research Center, Suzhou Institute of Nano-Tech and Nano-Bionics, Suzhou 215123, P. R. China*

Oskar J. Sandberg – *Physics and Center for Functional Materials, Faculty of Science and Technology, Åbo Akademi University, Turku 20500, Finland;* orcid.org/0000-0003-3778-8746

Rong Huang – *Vacuum Interconnected Nanotech Workstation, Suzhou Institute of Nano-Tech and Nano-Bionics, Suzhou 215123, P. R. China*

Zhiyun Li – *Vacuum Interconnected Nanotech Workstation, Suzhou Institute of Nano-Tech and Nano-Bionics, Suzhou 215123, P. R. China*

Ronald Österbacka – *i-Lab & Printable Electronics Research Center, Suzhou Institute of Nano-Tech and Nano-Bionics, Suzhou 215123, P. R. China; Physics and Center for Functional Materials, Faculty of Science and Technology, Åbo Akademi University, Turku 20500, Finland;* orcid.org/0000-0003-0656-2592

Complete contact information is available at: https://pubs.acs.org/10.1021/acsami.5c18226

Author Contributions

$^{\perp}$Q.X. and J.H. authors contributed equally.

Notes

The authors declare no competing financial interest.

■ ACKNOWLEDGMENTS

The authors would like to acknowledge the financial support from the National Natural Science Foundation of China (22075315,22579185), Suzhou Science and Technology

Foundation (SWY2022004). The authors are grateful for the technical support for Nano-X from the Suzhou Institute of Nano-Tech and Nano-Bionics, Chinese Academy of Sciences.

REFERENCES

(1) Zheng, X.; Zuo, L.; Yan, K.; et al. Versatile organic photovoltaics with a power density of nearly 40 W g−1. *Energy Environ. Sci.* **2023**, *16* (5), 2284−2294.
(2) Wang, J. X.; Han, C. Y.; Han, J. H.; Bi, F.; Sun, X.; Wen, S.; Yang, C.; Yang, C.; Bao, X.; Chu, J. Synergetic Strategy for Highly Efficient and Super Flexible Thick-film Organic Solar Cells. *Adv. Energy Mater.* **2022**, *12* (31), 2201614.
(3) Yang, S.; Chen, X.; Pan, Y.; Fang, J.; Han, Y.; Wang, Z.; Qian, F.; Qi, W.; Shui, K.; Zhang, Q.; et al. High Cell to Module Efficiency Remaining Ratio of ≈90% for the 100 cm^2 Fully Roll-to-Roll Gravure Printed Flexible Organic Solar Cells From Non-Halogenated Solvent. *Adv. Mater.* **2025**, *37* (17), 2500115.
(4) Li, C.; Cai, Y.; Hu, P.; et al. Organic Solar Cells with 21% Efficiency Enabled by a Hybrid Interfacial Layer with Dual-Component Synergy. *Nat. Mater.* **2025**, *24*, 1626−1634.
(5) Wang, L.; Chen, C.; Gan, Z.; Cheng, J.; Sun, Y.; Zhou, J.; Xia, W.; Liu, D.; Li, W.; Wang, T. Diluted Ternary Heterojunctions to Suppress Charge Recombination for Organic Solar Cells with 21% Efficiency. *Adv. Mater.* **2025**, *37*, 2419923.
(6) Zhu, L.; Zhang, M.; Zhou, G.; et al. Achieving 20.8% Organic Solar Cells via Additive-Assisted Layer-by-Layer Fabrication with Bulk p-i-n Structure and Improved Optical Management. *Joule* **2024**, *8*, 3153−3168.
(7) Ma, R.; Luo, Z.; Zhang, Y.; et al. Organic Solar Cells: Beyond 20%. *Sci. China Mater.* **2025**, *68* (6), 1689−1701.
(8) Wei, W.; Zhou, X.; Yang, M.; et al. A−D−A′−D−A-Type Non-Fused Ring Electron Acceptors for Organic Solar Cells and Photodetectors. *Sci. China Mater.* **2025**, *68* (1), 1−20.
(9) Ahmad, N.; Yuan, J.; Zou, Y.; et al. One More Step towards Better Stability of Non-Fullerene Organic Solar Cells: Advances, Challenges, Future Perspectives, and the Era of Artificial Intelligence. *Energy Environ. Sci.* **2025**, *18*, 5093−5158.
(10) Norrman, K.; Krebs, F. C. Lifetimes of organic photovoltaics:: Using TOF-SIMS and $^{18}O_2$ isotopic labelling to characterise chemical degradation mechanisms. *Sol. Energy Mater. Sol. Cells* **2006**, *90* (2), 213−227.
(11) Adams, J.; Salvador, M.; Lucera, L.; Langner, S.; Spyropoulos, G. D.; Fecher, F. W.; Voigt, M. M.; Dowland, S. A.; Osvet, A.; Egelhaaf, H.; et al. Water Ingress in Encapsulated Inverted Organic Solar Cells: Correlating Infrared Imaging and Photovoltaic Performance. *Adv. Energy Mater.* **2015**, *5* (20), 1501065.
(12) Yu, L. Y.; Qian, D. P.; Marina, S.; et al. Diffusion-Limited Crystallization: A Rationale for the Thermal Stability of Non-Fullerene Solar Cells. *ACS Appl. Mater. Interfaces* **2019**, *11* (24), 21766−21774.
(13) Han, Y. F.; Hu, Z. S.; Zha, W. S.; Chen, X.; Yin, L.; Guo, J.; Li, Z.; Luo, Q.; Su, W.; Ma, C. 12.42% Monolithic 25.42 cm^2 Flexible Organic Solar Cells Enabled by an Amorphous ITO-Modified Metal Grid Electrode. *Adv. Mater.* **2022**, *34* (17), 2110276.
(14) Yan, L. P.; Gu, H. M.; Li, Z. R.; et al. The Interfacial Degradation Mechanism of Polymer:Fullerene Bis-Adduct Solar Cells and Their Stability Improvement. *Mater. Adv.* **2020**, *1* (5), 1307−1317.
(15) Liu, B. W.; Su, X.; Lin, Y.; Li, Z.; Yan, L.; Han, Y.; Luo, Q.; Fang, J.; Yang, S.; Tan, H.; et al. Simultaneously Achieving Highly Efficient and Stable Polymer:Non-Fullerene Solar Cells Enabled by Molecular Structure Optimization and Surface Passivation. *Adv. Sci.* **2022**, *9* (7), 2104588.
(16) Qin, J.; Wu, N.; Chen, W.; Liu, B.; Wang, Z.; Zhang, L.; Yin, N.; Chen, Q.; Zhang, Z.; Ma, C. In Situ Solution-Processed Submicron Thick SiO_xC_y/a-SiN_x(O):H Composite Barrier Film for Polymer:Non-Fullerene Photovoltaics. *Small Methods* **2023**, *7* (7), 2300224.
(17) Li, Y.; Liu, K.-K.; Lin, F. R.; Jen, A. K. Y. Improving the stability of organic solar cells: From materials to devices. *Sol. RRL* **2023**, *7* (20), 2300531.
(18) Liu, C.; Xiao, C.; Li, W.; et al. Zinc Oxide Nanoparticles as Electron Transporting Interlayer in Organic Solar Cells. *J. Mater. Chem. C* **2021**, *9* (40), 14093−14114.
(19) Garcia Romero, D.; Di Mario, L.; Loi, M. A.; et al. Tin Oxide: The Next Benchmark Transport Material for Organic Solar Cells? *ACS Energy Lett.* **2025**, *10* (3), 1330−1337.
(20) Li, Y.; Zhou, D.; Han, L.; Quan, J.; Wang, F.; Yang, X.; Hu, L.; Wang, J.; Xu, H.; Chen, L. N-Type Small Molecule Electron Transport Layers with Excellent Surface Energy and Moisture Resistance Siloxane for Non-Fullerene Organic Solar Cells. *Small* **2024**, *20* (19), 2308961.
(21) Liu, B. W.; Han, Y. F.; Li, Z. R.; Gu, H.; Yan, L.; Lin, Y.; Luo, Q.; Yang, S.; Ma, C. Q. Visible Light-Induced Degradation of Inverted Polymer: Nonfullerene Acceptor Solar Cells: Initiated by the Light Absorption of ZnO Layer. *Sol. RRL* **2021**, *5* (1), 2000638.
(22) Lai, X.; Chen, S. Y.; Gu, X. Y.; Lai, H.; Wang, Y.; Zhu, Y.; Wang, H.; Qu, J.; Kyaw, A. K. K.; Xia, H.; et al. Phenanthroline-carbolong interface suppress chemical interactions with active layer enabling long-time stable organic solar cells. *Nat. Commun.* **2023**, *14* (1), 3571.
(23) Mai, T. L. H.; Jeong, S.; Kim, S.; Jung, S.; Oh, J.; Sun, Z.; Park, J.; Lee, S.; Kim, W.; Yang, C. Over 18.2%-Efficiency Organic Solar Cells with Exceptional Device Stability Enabled by Bay-Area Benzamide-Functionalized Perylene Diimide Interlayer. *Adv. Funct. Mater.* **2023**, *33* (36), 2303386.
(24) Zhao, B.; Huang, X.; Chung, S.; et al. Hole-Selective-Molecule Doping Improves the Layer Thickness Tolerance of PEDOT:PSS for Efficient Organic Solar Cells. *eScience* **2025**, *5* (1), 100305.
(25) Zhao, Y.; Yu, L. M.; Sun, M. L. Recent progress in emerging 2D layered materials for organic solar cells. *Sol. Energy* **2021**, *218*, 621−638.
(26) Jiang, F.; Choy, W. C. H.; Li, X.; et al. Post-Treatment-Free Solution-Processed Non-Stoichiometric NiO_x Nanoparticles for Efficient Hole-Transport Layers of Organic Optoelectronic Devices. *Adv. Mater.* **2015**, *27* (18), 2930−2937.
(27) Lin, Y.; Magomedov, A.; Firdaus, Y.; et al. 18.4% Organic Solar Cells Using a High Ionization Energy Self-Assembled Monolayer as Hole-Extraction Interlayer. *ChemSusChem* **2021**, *14* (17), 3569−3578.
(28) Yu, X.; Xi, Q.; Qin, J.; et al. Unexpected MoO_3/Al Interfacial Reaction Lowering the Performance of Organic Solar Cells upon Thermal Annealing and Methods for Suppression. *ACS Appl. Mater. Interfaces* **2025**, *17* (17), 25419−25428.
(29) Xi, Q.; Qin, J.; Sandberg, O. J.; et al. Improving the Thermal Stability of Inverted Organic Solar Cells by Mitigating the Undesired MoO3 Diffusion toward Cathodes with a High-Ionization Potential Interface Layer. *ACS Appl. Mater. Interfaces* **2025**, *17* (10), 15456−15467.
(30) Lee, S.; Jin, J. S.; Moon, H.; et al. Long-Term Thermal Stability of Nonfullerene Organic Solar Cells via Facile Self-Assembled Interface Passivation. *ACS Energy Lett.* **2023**, *8* (10), 3989−3998.
(31) Qin, X.; Yu, X.; Li, Z.; et al. Thermal-Induced Performance Decay of the State-of-the-Art Polymer: Non-Fullerene Solar Cells and the Method of Suppression. *Molecules* **2023**, *28*, 6856.
(32) Yao, H.; Ye, L.; Hou, J.; Jang, B.; Han, G.; Cui, Y.; Su, G. M.; Wang, C.; Gao, B.; Yu, R.; et al. Achieving highly efficient nonfullerene organic solar cells with improved intermolecular interaction and open-circuit voltage. *Adv. Mater.* **2017**, *29* (21), 1700254.
(33) Liu, H.; Liu, Z.-X.; Wang, S.; Huang, J.; Ju, H.; Chen, Q.; Yu, J.; Chen, H.; Li, C. Boosting Organic−Metal Oxide Heterojunction via Conjugated Small Molecules for Efficient and Stable Nonfullerene Polymer Solar Cells. *Adv. Energy Mater.* **2019**, *9* (34), 1900887.
(34) Mihailetchi, V. D.; Koster, L. J. A.; Hummelen, J. C.; et al. Photocurrent Generation in Polymer-Fullerene Bulk Heterojunctions. *Phys. Rev. Lett.* **2004**, *93* (21), 216601.

https://doi.org/10.1021/acsami.5c18226
ACS Appl. Mater. Interfaces 2025, 17, 66673−66682

(35) Zhu, C.; Tian, J.; Liu, W.; et al. Batch-Reproducible and Thickness-Insensitive Mesopolymer Zwitterion Interlayers for Organic Solar Cells. *ACS Energy Lett.* **2023**, *8* (6), 2689−2698.
(36) Wöpke, C.; Göhler, C.; Saladina, M.; Du, X.; Nian, L.; Greve, C.; Zhu, C.; Yallum, K. M.; Hofstetter, Y. J.; Becker-Koch, D.; et al. Traps and transport resistance are the next frontiers for stable nonfullerene acceptor solar cells. *Nat. Commun.* **2022**, *13* (1), 3786.

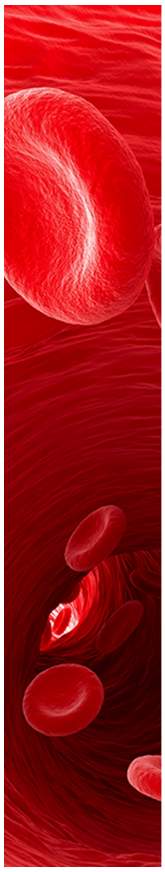
CAS BIOFINDER DISCOVERY PLATFORM™
CAS BIOFINDER HELPS YOU FIND YOUR NEXT BREAKTHROUGH FASTER
Navigate pathways, targets, and diseases with precision
Explore CAS BioFinder
CAS
A division of the American Chemical Society

https://doi.org/10.1021/acsami.5c18226
ACS Appl. Mater. Interfaces 2025, 17, 66673−66682